



## Article

# An Investigation of the Lower Stratospheric Gravity Wave Activity in Tibetan Plateau Based on Multi-GNSS RO Dry Temperature Observations

Zhiping Chen <sup>1,2,3,4,\*</sup>, Yu Gao <sup>2</sup>, Li Li <sup>2</sup>, Xiaoxing He <sup>5</sup> , Weifeng Yang <sup>2</sup>, Haowen Luo <sup>2</sup>, Xunqiang Gong <sup>2,4</sup> and Kaiyun Lv <sup>2,4</sup>

- <sup>1</sup> Key Laboratory for Digital Land and Resources of Jiangxi Province, East China University of Technology, Nanchang 330013, China
- <sup>2</sup> Faculty of Geomatics, East China University of Technology, No. 148, Guanglan Ave., Nanchang 330013, China
- <sup>3</sup> State Key Laboratory of Geodesy and Earth's Dynamics, Innovation Academy for Precision Measurement Science and Technology, Chinese Academy of Sciences, Wuhan 430077, China
- <sup>4</sup> Key Laboratory of Mine Environmental Monitoring and Improving around Poyang Lake, Ministry of Natural Resources, Nanchang 330013, China
- <sup>5</sup> School of Civil and Surveying & Mapping Engineering, Jiangxi University of Science and Technology, Ganzhou 341000, China
- \* Correspondence: zhpchen@ecut.edu.cn; Tel.: +86-199-7995-6889



**Citation:** Chen, Z.; Gao, Y.; Li, L.; He, X.; Yang, W.; Luo, H.; Gong, X.; Lv, K. An Investigation of the Lower Stratospheric Gravity Wave Activity in Tibetan Plateau Based on Multi-GNSS RO Dry Temperature Observations. *Remote Sens.* **2022**, *14*, 5671. <https://doi.org/10.3390/rs14225671>

Academic Editors: Vagner Ferreira, Balaji Devaraju, Peng Yuan and Liangke Huang

Received: 16 October 2022

Accepted: 7 November 2022

Published: 10 November 2022

**Publisher's Note:** MDPI stays neutral with regard to jurisdictional claims in published maps and institutional affiliations.



**Copyright:** © 2022 by the authors. Licensee MDPI, Basel, Switzerland. This article is an open access article distributed under the terms and conditions of the Creative Commons Attribution (CC BY) license (<https://creativecommons.org/licenses/by/4.0/>).

**Abstract:** To understand the activity of gravity waves (GWs) over the Tibetan Plateau (TP) is of great significance for improving global climate models. Considering that the lower stratosphere is the main level of GWs activity, this paper first established a 14-year  $2^\circ \times 2^\circ$  longitude–latitude monthly mean GWs model in the lower stratosphere (18~20 km) of the TP by combining post-processed dry temperature profiles provided by the multi-Global Navigation Satellite System (GNSS) radio occultation (RO) missions: The Constellation Observing System for Meteorology, Ionosphere, and Climate (COSMIC) and the Meteorological Operational (METOP) series polar-orbiting meteorological satellites (METOP-A, METOP-B, and METOP-C) from August 2006 to September 2020. Based on this model, this paper analyzed the characteristics of GWs activity around TP and the effects of topography, background wind, and zonal wind on GWs activity and summarized the general process of topographic wave excitation and upward propagation around TP. The spatial distribution of the lower stratospheric GW  $E_p$  is highly correlated with the spatial distribution of background wind and the topography of TP during GWs excitation. The GW  $E_p$  is obviously filtered by the zero-speed wind. The change in GW  $E_p$  is strongly correlated with the change in topography. These phenomena indicate that the GWs of TP are mainly topographic waves. Moreover, the lower stratospheric GW  $E_p$  of TP shows that periodic changes are mainly affected by the periodic background wind, and the GW  $E_p$  value is larger in February and smaller in August. The large GW  $E_p$  in the lower stratosphere of TP is not only related to the GWs strongly generated by the interaction between the strong background wind and the large elevation or large topographic changes but also related to the strong zonal westerly winds that promote the propagation of GWs upward. Multivariable linear regression models were used to reconstruct the lower stratospheric GW  $E_p$  over TP based on the background wind and the zonal wind and a goodness of fit of 81.1% was achieved. It indicates that the GW  $E_p$  is dominated by the topographic wave over TP in the lower stratosphere and the background wind has a greater influence on the GWs than the zonal wind.

**Keywords:** gravity wave; multi-GNSS radio occultation; Tibetan Plateau; topography; background wind

## 1. Introduction

Atmospheric gravity waves (GWs) have an important influence on global atmospheric circulation and the dynamic and thermodynamic structure of the atmosphere [1–4]. The

generation of GWs is related to topography, convection, wind shear, and geostrophic adaptation [5–7]. Hoffmann et al. [8] studied the GW activity in global hotspots and showed that most GW sources in active regions were related to mountains or convective. In addition, Zeng et al. [9] pointed out that orographic excitation is one of the more common sources of vertically propagating GWs. Considering the global influence of GWs on atmospheric circulation, GW parameters should be introduced into global climate models used for climate and meteorological forecasting [10]. Therefore, obtaining high-precision topographic wave parameters by various observation means and calculation methods [11–13] and analyzing the activity characteristics and generation mechanism of topographic wave can provide effective constraints for GW parameterization and improve the prediction accuracy and reliability of the model.

The lower stratosphere is not only the main level of GW activity but also the altitude level with close material and energy exchange, especially for the Tibetan Plateau (TP). Known as the ‘roof of the world’, the TP is surrounded by the Himalayas, Hengduan Mountains, and Kunlun Mountains, with a total length of approximately 2800 km from east to west. This is one of the most complex landforms in the world and an important source of atmospheric GWs [8]. Xu et al. [14] pointed out that the topography of the TP mainly affects the GWs activity in the lower stratosphere. Wei et al. [15] analyzed the impact of topographic waves on the material exchange between the upper troposphere and the lower stratosphere on the TP and found that the breaking of topographic waves would lead to a low-value area of potential vorticity and ozone in the lower stratosphere, and the Brunt–Väisälä frequency also appeared in an abnormally low-value area in the lower stratosphere due to the impact of the topographic wave process. Zeng et al. [9] pointed out that in spring and winter when zonal winds are westerly winds exceeding 10 m/s, the topographic waves of TP may propagate upward in the whole lower stratosphere. However, these studies are not specific enough regarding GWs activity and the effect of topography on GWs activity in the lower stratosphere. In addition, Zeng et al. [9] pointed out that the topographic wave activity of TP may not be recognized in previous studies due to the use of short time scales and different wave activity proxies. Therefore, there is a lack of research on the generation mechanism of topographic waves over TP. At present, the whole process of topographic wave generation and upward propagation into the middle atmosphere is not well understood.

With the successful implementation of the global navigation satellite system (GNSS) radio occultation (RO) missions, GNSS RO technology has gradually become the main means to detect atmospheric GWs [16,17]. For example, COSMIC (Constellation Observing System for Meteorology, Ionosphere, and Climate) was launched jointly by the United States Department of Defense and the Taiwan of China and METOP (the Meteorological Operational) series polar orbiting meteorological satellites (METOP-A, METOP-B, and METOP-C) were launched by Europe. Compared with other detection methods, GNSS RO technology has the characteristics of all-weather global coverage, self-calibration, long-term stability, high precision, good vertical resolution, and low cost in the detection of atmospheric parameter profiles [18–23]. The temperature profile provided by COSMIC has an accuracy of  $\pm 0.5$  K between 5 and 30 km [24,25], and the accuracy of METOP series satellites is  $\pm 1$  K when there is no cloud. Khaniani [26] compared the temperature data (2006–2018) provided by several GNSS RO missions from COSMIC, METOP-A, and METOP-B with radiosonde and showed the temperature bias between them was within  $\pm 1.5$  K below 28 km. These results show that the dry temperature profile provided by GNSS RO missions has high accuracy and meets the requirements of GW extraction. At present, the studies on GWs are mainly based on the observations provided by a single GNSS RO mission. For example, Hei et al. [19] analyzed the characteristics of GW activity over the polar region with a grid resolution of  $20^\circ \times 10^\circ$  longitude–latitude based on the CHAMP observations from 2001 to 2005; Liang et al. [20] revealed the global distribution characteristics of stratospheric GWs with a grid resolution of  $15^\circ \times 10^\circ$  longitude–latitude based on the COSMIC observations from 2007 to 2012. These research studies have limitations regarding the

length of time and the resolution of GWs to some extent. Furthermore, the short time scale is not conducive to the observation of topographic waves [9,27]. Therefore, the combination of multi-GNSS RO missions is necessary for the specific study of GW activity, especially for such a topographic-wave-dominated region as the TP. On the one hand, the combination of multi-GNSS RO missions can increase the number of observations and improve the resolution of GWs. On the other hand, increasing the time scale of the study can reduce the influence of individual special events on the results, improve the reliability of the results, and facilitate the study of the long-term variation characteristics of GWs.

In this paper, the combination of dry temperature profiles of the multi-GNSS RO (COSMIC, METOP-A, METOP-B, and METOP-C) missions from August 2006 to September 2020 was used to model GWs over the TP for 14 years. Based on this model, we analyze the characteristics of GW activity and the effect of topography on GW activity in the lower stratosphere. In addition, the reason for the periodic variation of GWs in the lower stratosphere and the influence of background winds during excitation and zonal winds during upward propagation on GWs in the lower stratosphere are analyzed. In order to quantify this effect, a multivariable linear regression model is used to reconstruct the GWs in the lower stratosphere over the TP. Finally, the general process of interaction between the background wind and the topography to excite topographic waves and topographic waves propagating upward under the influence of the zonal wind over the TP is summarized.

The manuscript is organized as follows. In Section 2, a  $2^\circ \times 2^\circ$  longitude–latitude monthly mean GW model was established, the accuracy and stability of the RO temperature were analyzed, and the GW potential energy (Ep) of the TP was extracted. In Section 3, the vertical and spatial distribution of GW Ep and the correlation between the topography and the GW Ep in the TP are analyzed. Moreover, the factors that cause the periodic change and spatial distribution of the GW Ep in the lower stratosphere are investigated. Then, multivariable linear regression models are used to reconstruct the GW Ep in the lower stratosphere, and the general process of topographic wave excitation and upward propagation is summarized. The conclusions are presented in Section 4.

## 2. Datasets and Methods

### 2.1. Multi-GNSS RO Observations

The study of GWs requires long-time-scale, high-resolution, and high-precision GW parameters, especially for the TP where topographic waves are generated by a complex topography. This paper used the dry temperature profiles retrieved from four GNSS RO missions: COSMIC, METOP-A, METOP-B, and METOP-C, provided by the COSMIC Data Analysis and Archive Center (CDAAC) from August 2006 to September 2020. A  $2^\circ \times 2^\circ$  monthly mean GW model around the TP was established to study the GW activities. In order to obtain the obvious GW activity over the TP ( $25\sim 41^\circ\text{N}$ ,  $68\sim 105^\circ\text{E}$ ), the surrounding area of the TP was also taken into account. Figure 1 presents the number of RO events around the TP ( $20\sim 50^\circ\text{N}$ ,  $60\sim 120^\circ\text{E}$ ) for each mission. Figure 1 notes that COSMIC provides a large number of daily RO events during its stable operation, with a maximum of 120, while the number of daily RO events provided by COSMIC at the beginning and end is less than 20. The daily numbers of RO events provided by the METOP series are stable at approximately 20. The mean number of daily RO events is approximately 71, and the mean number of monthly RO events is approximately 2137. Notably, the total number of daily RO events was lower than 20 from May to July 2006, which was not enough to establish the monthly mean GW model of  $2^\circ \times 2^\circ$ , so this time period was not considered.

Leroy et al. [28] pointed out that biases may be introduced when the combined datasets were from different GNSS RO observations. In order to analyze the bias between COSMIC and METOP series observations, Figure 2 shows the monthly time series of temperature and temperature bias of 8–38 km around the TP from May 2006 to September 2020, respectively. The time series of dry temperatures provided by different GNSS RO missions are consistent (Figure 2a). The temperature bias between each RO mission and the average temperature of the COSMIC and METOP series observations during the operation period from April 2006

to September 2020 is small and stable within  $\pm 0.4$  K, except for COSMIC after April 2018 (Figure 2b). After April 2018, COSMIC showed a large temperature bias with a maximum of 0.9 K. In addition, COSMIC only provided RO events in January and February 2019 and January to April 2020, and the number of RO events is small (Figure 1). Therefore, the COSMIC observations after April 2018 are not considered.

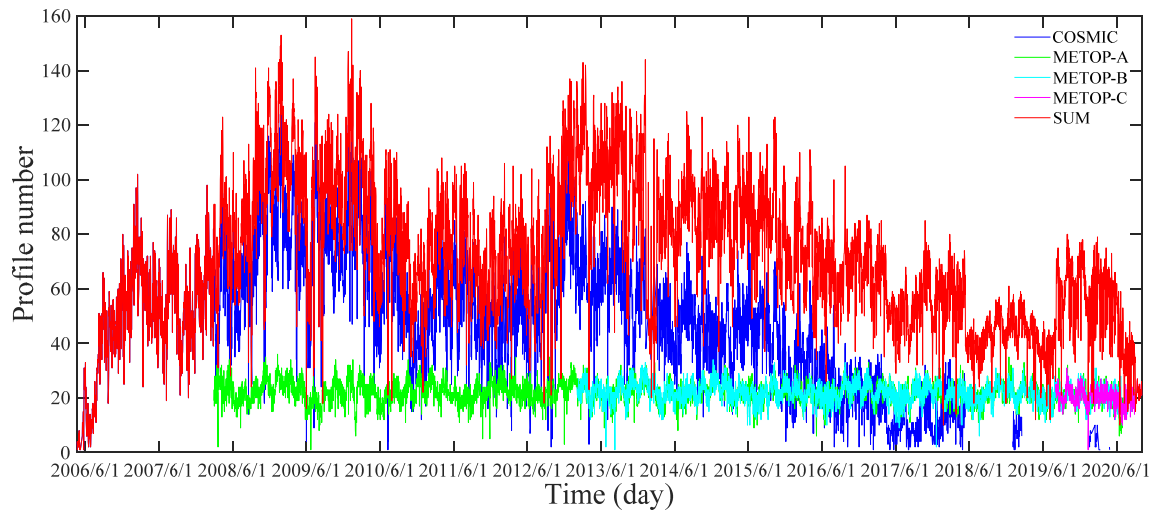


**Figure 1.** The number of GNSS RO events of each mission around the TP ( $20\sim 50^{\circ}\text{N}$ ,  $60\sim 120^{\circ}\text{E}$ ) from May 2006 to September 2020. The red solid line indicates the total number of GNSS RO events provided by the selected missions in this paper. Blue solid line, the number of COSMIC GNSS RO events; green solid line, the number of METOP-A GNSS RO events; cyan solid line, the number of METOP-B GNSS RO events; magenta solid line, the number of METOP-C GNSS RO events.

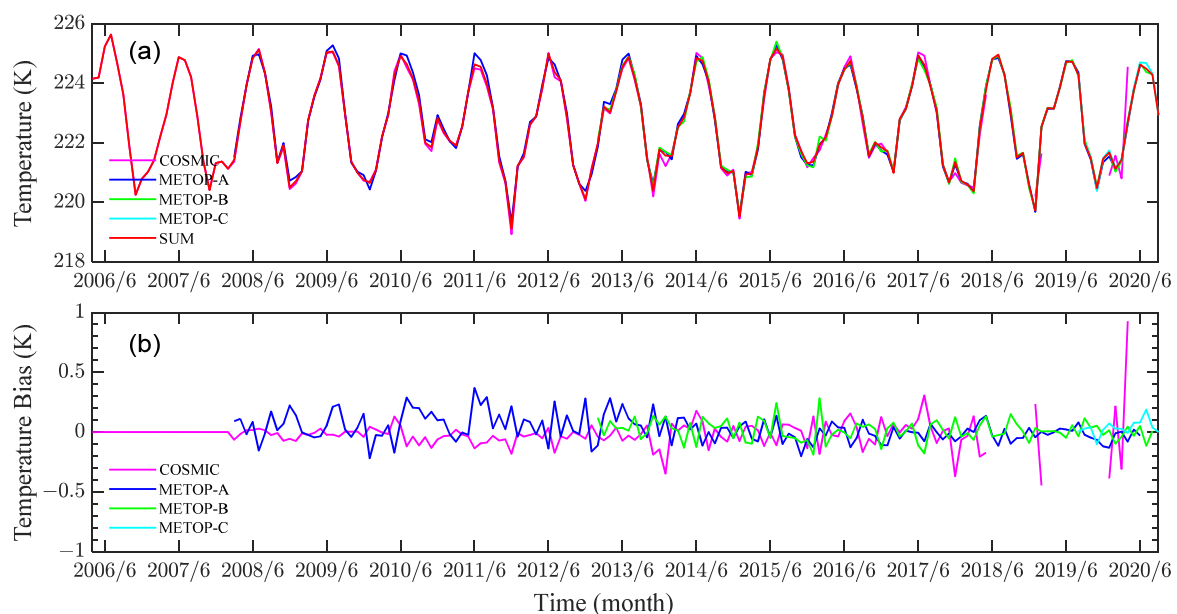


**Figure 2.** The monthly average of (a) temperature and (b) the temperature bias variation of  $8\sim 38$  km around TP ( $20\sim 50^{\circ}\text{N}$ ,  $60\sim 120^{\circ}\text{E}$ ) from May 2006 to September 2020. Magenta solid line, the COSMIC temperature; blue solid line, the METOP-A temperature; green solid line, the METOP-B temperature; cyan solid line, the METOP-C temperature; red solid line, the combined temperature.

The number of RO events before July 2006 was only provided by COSMIC, which was too small to establish the monthly mean GW model of  $2^{\circ} \times 2^{\circ}$ . In addition, the temperature bias of COSMIC after April 2018 was large. Therefore, the observations from COSMIC before July 2006 and after April 2018 were not considered. The number of RO events

provided by the METOP series is stable and the temperature bias is small during their operation. As shown in Table 1, according to the operation time of different METOP RO missions, this paper combined the dry temperature of COSMIC from August 2006 to April 2018 with the dry temperature of METOP series RO missions. We took the RO events of January 2015 as an example to draw the distribution of RO events over the studied area as shown in Figure 3. The RO events almost cover all grids ( $2^\circ \times 2^\circ$ ), and the grid coverage reaches 99.77%, which was 100% in TP ( $25^\circ\text{--}41^\circ\text{N}$ ,  $68^\circ\text{--}105^\circ\text{E}$ ). Figure 4 shows the monthly coverage of GNSS RO events of the TP and its surrounding areas divided by a  $2^\circ \times 2^\circ$  grid from August 2006 to September 2020. From Figure 4, the grid coverage of TP and its surrounding areas is over 90% almost every month, and the monthly grid coverage from June 2008 to June 2017 is close to 100%. The monthly mean grid coverage from August 2006 to September 2020 is 97.86%, which is 97.33% in the TP. These indicate that it is feasible to establish a  $2^\circ \times 2^\circ$  monthly mean GWs model using the combination of multi-GNSS RO observations.

**Table 1.** The selected RO missions in each time interval around TP from August 2006 to September 2020.

Time Interval	Satellite
August 2006 (213)~February 2008 (060)	COSMIC
March 2008 (061)~January 2013 (031)	COSMIC, METOP-A
February 2013 (032)~April 2018 (120)	COSMIC, METOP-A, METOP-B
May 2018 (121)~July 2019 (212)	METOP-A, METOP-B
August 2019 (213)~June 2020 (182)	METOP-A, METOP-B, METOP-C
July 2020 (183)~August 2020 (246)	METOP-B, METOP-C
September 2020 (247)~September 2020 (274)	METOP-C

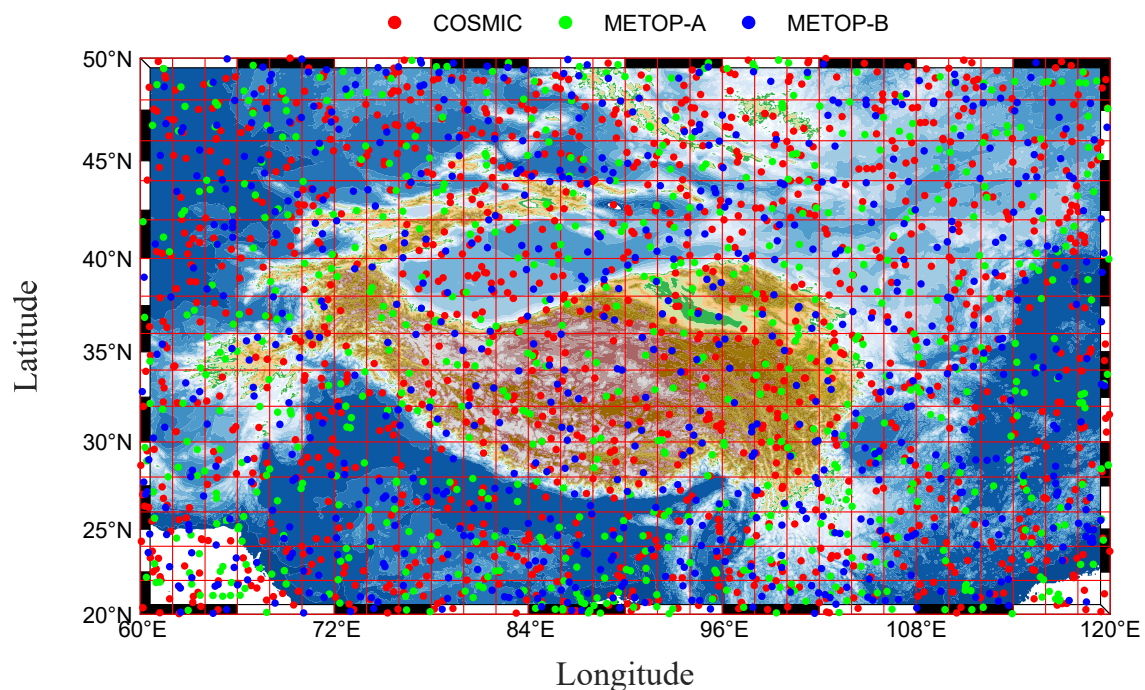


**Figure 3.** The distribution of RO events around TP ( $20^\circ\text{--}50^\circ\text{N}$ ,  $60^\circ\text{--}120^\circ\text{E}$ ) in January 2015. Red dot, COSMIC RO event; green dot, METOP-A RO event; blue dot, METOP-B RO event.

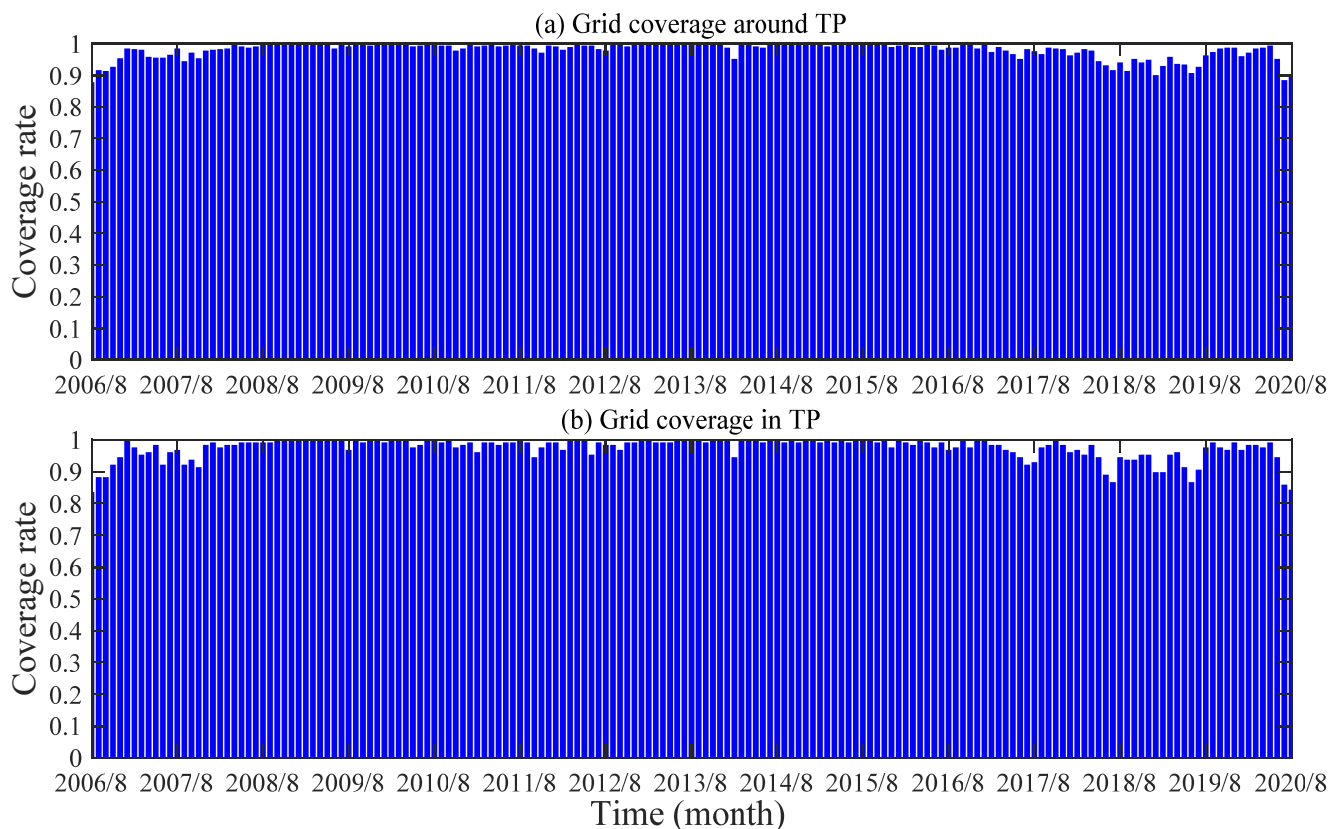


**Figure 4.** The monthly grid ( $2^{\circ} \times 2^{\circ}$ ) coverage of GNSS RO events (a) around TP ( $20^{\circ}\sim 50^{\circ}\text{N}$ ,  $60^{\circ}\sim 120^{\circ}\text{E}$ ) and (b) in ( $25^{\circ}\sim 41^{\circ}\text{N}$ ,  $68^{\circ}\sim 105^{\circ}\text{E}$ ) the TP from August 2006 to September 2020.

In order to ensure the reliability of GWs, the monthly mean temperature, the temperature bias, and the temperature trend of different RO missions, which vary with altitude at 8~38 km around the TP, are presented in Figure 5. From Figure 5a, the values of temperature from different RO missions at the altitude of 8~38 km are consistent. The temperature bias of METOP-A and METOP-B is stable at approximately 0 at 8~38 km. A large temperature bias appears below 14 km of COSMIC and METOP-C, within 0.2 K and 0.4 K, respectively (Figure 5b). These indicate that the temperature bias between the different RO missions and their combination is small. Due to periodic changes in temperature data, the trend values are affected by the time lengths, and a large time length corresponds to a small trend. Since the METOP-C (August 2019–September 2020) observations used in this paper were only 14 months, the observation of other RO missions with the same time length (August 2014–September 2015) is selected for comparison. Figure 5c shows that the temperature trends from different RO missions at the altitude of 8~38 km are similar, and all of them are stable within  $\pm 0.5$  K/month. In addition, the temperature trends within the time range of COSMIC, METOP-A, and METOP-B shown in Table 1 were calculated, and the temperature bias of different RO missions were all approximately 0 within the altitude of 8~38 km. These indicate that the temperatures provided by the different RO missions selected in Table 1 are reliable and stable and can be used for high-precision GW extraction.

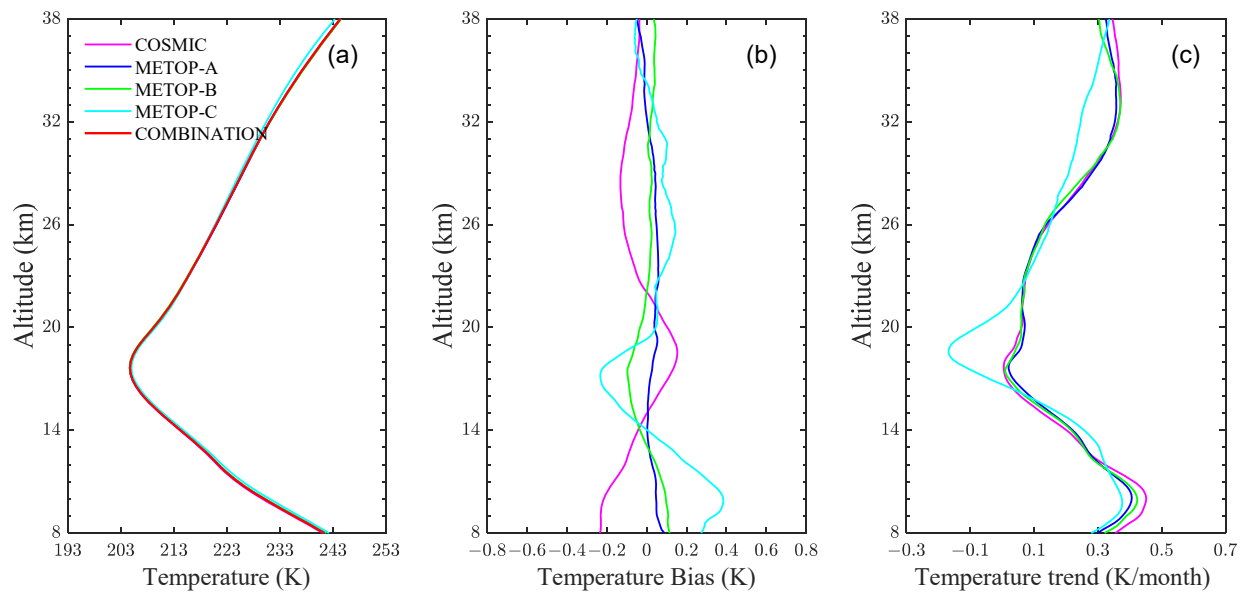


**Figure 5.** The (a) temperature, (b) temperature bias, and (c) temperature trend in each RO mission varying with altitude at 8~38 km. Magenta solid line, the COSMIC temperature; blue solid line, the METOP-A temperature; green solid line, the METOP-B temperature; cyan solid line, the METOP-C temperature; red solid line, the combined temperature.

## 2.2. The Wind Datasets

In this study, we used the monthly mean reanalysis data for zonal wind and meridional wind obtained from the ERA5 database (<https://cds.climate.copernicus.eu/cdsapp#!/dataset/> (accessed on 16 July 2022)) to specifically study the interaction between the topography and the wind fields from August 2006 to September 2020. The ERA5 database provides reanalysis data of various atmospheric parameters available from 1979 to the present day provided by the European Center for Medium-range Weather Forecasts (ECMWF) [29]. The data are distributed in a horizontal grid of  $0.25^\circ \times 0.25^\circ$  (longitude  $\times$  latitude) at 37 vertical pressure levels extending from 1000 to 1 hPa (~0–45 km). At the same height, the background wind (horizontal direction) with the same horizontal resolution ( $0.25^\circ \times 0.25^\circ$ ) can be obtained by the sum of meridional and zonal wind vectors in the same position.

## 2.3. The Extraction of GW Ep

GNSS RO technology is considered active satellite-to-satellite telemetry technology. When the radio signal passes through the neutral atmosphere, there is a phase delay between the receiver and transmitter [18,30,31]. The Doppler frequency shift was calculated by the phase delay, and the bending angle profile was obtained by combining the position and velocity of the LEO satellite [30,31]. The refractive index profile is obtained from the bending angle profile through ionosphere optimization, bending angle statistical optimization, and Abel integral transformation [31]. If the effects of electron density and water droplets are ignored, the atmospheric refractive index can be expressed as Formula (1); if the effects of atmospheric water vapor continue to be ignored, as in Formula (2) [31], the dry temperature profile of GW Ep extracted in this paper can be obtained.

$$N = (n - 1) \times 10^6 = 77.6 \frac{P}{T} + 3.73 \times 10^5 \frac{P_W}{T^2} \quad (1)$$

$$T_{dry} = 77.6 \frac{P}{N} \quad (2)$$

Liang et al. [20] pointed out that the GW Ep can indicate the activity intensity of GWs. The dry temperature profile from different RO missions in Table 1 was used to calculate the GW Ep, and the calculation formula is as follows [11,12,32]:

$$E_p = \frac{1}{2} \left( \frac{g}{N} \right)^2 \left( \frac{T'}{\bar{T}} \right)^2 \quad (3)$$

$$N^2 = \frac{g}{\bar{T}} \left( \frac{\partial \bar{T}}{\partial z} + \frac{g}{C_p} \right) \quad (4)$$

$$T' = T - \bar{T} \quad (5)$$

In Formula (3),  $g$  is the gravity acceleration,  $N$  is the Brunt–Väisälä frequency,  $T'(K)$  is the temperature perturbation caused by GWs,  $\bar{T}(K)$  is the background temperature,  $C_p$  in Formula (4) represents the isobaric heating capacity,  $g/C_p = 9.8 \times 10^{-3} \text{ K/m}$  represents the adiabatic temperature drop rate,  $z(m)$  represents height, and  $T$  in Formula (5) represents the raw temperature.

According to the above formula, the temperature perturbation caused by GWs is the key to obtaining GW Ep. Cai et al. [11] used a least-squares fitting approach to obtain the temperature perturbation from Lidar data at 84–89 km. Yang et al. [12] used a 2–10 km band-stop filter to acquire the temperature perturbation from ERA5 Reanalysis Data at 5–75 km. Xu et al. [14] used horizontal filtering on the temperature profile to attain the temperature perturbations from COSMIC RO data at 15–31 km. Furthermore, the horizontal filtering of the temperature profile can better eliminate the influence of other large-scale waves in temperature perturbation [14]. Therefore, we used the method of Xu et al. [14] to extract GW Ep in this study. Specifically, we divided the daily temperature profile into  $2^\circ \times 2^\circ$  grids to obtain the mean grid temperature, and the mean grid temperature in the vertical direction was interpolated by 0.2 km. Then, S-transform and 0–6 zonal wavenumber filtering were used on the mean grid temperature to obtain the background temperature. Further, the temperature perturbation is obtained by Formula (5). Finally, the GW Ep is calculated according to Formulas (3) and (4). To ensure that the GW Ep values are credible and caused by GWs, we compare our results with those of Zeng et al. [9] and find them to be similar.

### 3. Results and Discussion

Based on the established  $2^\circ \times 2^\circ$  monthly mean GWs model in Section 2, this section analyzes the activity characteristics of GWs, the correlation between topography and GWs, and the reason for the periodicity and spatial distribution of GWs. Then, the GWs in the lower stratosphere of the TP are reconstructed. The excitation and propagation processes of topographic waves are summarized.

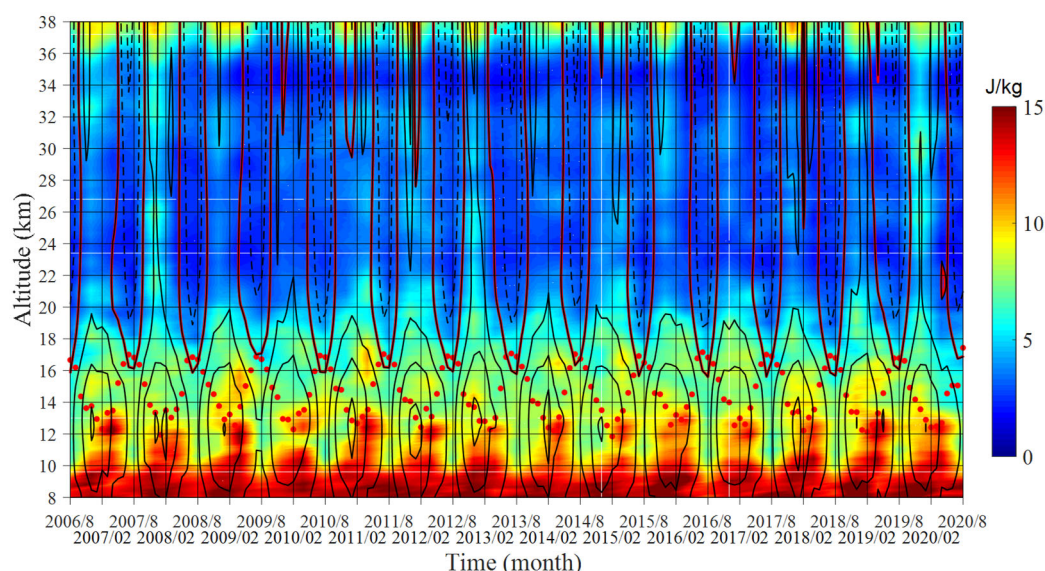
#### 3.1. Time-Altitude Distribution of GW Ep

Figure 6 describes the vertical distribution of the monthly mean GW Ep over the TP with an altitude of 8–38 km from August 2006 to September 2020. It is shown that the GW Ep, zonal winds, and tropopause have periodic changes over TP. At the same altitude, the GW Ep reaches its maximum when the westerly wind is strong around February and reaches its minimum when the westerly wind is weak or easterly around August [33].

From Figure 6, the GW Ep over TP has a vertical distribution that decreases first and then increases. In months with no reversal of the wind direction, the GWs propagate upward under the strong westerly winds at altitudes below 20 km and the GW Ep is larger as a whole. At the altitude of 20–36 km, the value of GW Ep is small, which may be related to the weak westerly wind [34]. These results indicate that the strong westerly winds over TP are conducive to the upward propagation of GWs [34–37]. The value of GW Ep above 36 km is larger due to the influence of the strong westerly winds [25,34]. In the month of the wind direction reversal, the GWs propagate upward under the strong westerly wind and the GW Ep is large below the zero-speed wind height. With the increase in altitude,

the value of GW Ep near the zero-speed wind decreases sharply, which is due to the fact that the quasi-static GWs caused by the topography are filtered out after reaching a critical height [1,20]. The result indicates the existence of topographic waves around the TP. At a height above the zero-speed wind, the GWs continue to propagate upward under the easterly wind, and the value of GW Ep is small.

The strong GW activity in the TP is beneficial to the study of GWs' activity characteristics and the generation and propagation process of topographic waves. Khaykin et al. [38] pointed out that the wave-induced fluctuations cause abrupt changes in the structure of the tropopause, and the values of the GW Ep of this layer will likely be overestimated. Therefore, the GW Ep at altitudes below the tropopause (~17 km) is not credible, and this study mainly focuses on altitudes above 17 km. As seen in Figure 6, when the wind direction did not reverse in winter, the height of strong GW activity was mainly concentrated below 20 km. When the wind direction reverses in summer, the GWs' activity above 18 km is significantly weakened by the influence of zero-speed wind [35,37]. Therefore, in order to specifically study the GWs' activity characteristics and the periodic change in GWs around the TP, an altitude of 18~20 km is selected for the following study.



**Figure 6.** The vertical distribution of the monthly mean GW Ep over TP (25~41°N, 68~105°E) at 8~38 km from August 2006 to September 2020. The red solid dot represents the Lapse Rate Tropopause, the black solid line represents the westerly wind, the black dotted line represents the east wind, the red solid line represents the zero-speed wind, and the zonal wind data are provided by the ERA5.

### 3.2. Spatial Distribution of GW Ep and Background Wind

The blocking of background wind by topography is the main way to generate GWs around TP [9]. Figure 7 shows the spatial distribution of the GW Ep and the background wind around the TP. From Figure 7, the background wind and the GW Ep have similar periodic changes. The largest value of GW Ep appears from November to March when the background wind is strong, and the smallest value appears in July, August, and September when the background wind is weak. It is worth noting that from November to March, there is a large GW Ep at the edge of the TP [14], which mainly exists in the southeast of the TP where the background wind is strong. This may be due to the strong background wind being blocked by the topography at the edge, which promoted the generation of GWs. In June, July, and August, there is a large GW Ep in the latitudes of 20°N to 30°N, which may be related to the tropical convection [17,20,33,34]. In general, the spatial distribution of the GW Ep in the lower stratosphere is highly correlated with the spatial distribution of

background wind and the topography of the TP, indicating that topographic waves are generated around the TP and propagate upward to the lower stratosphere.

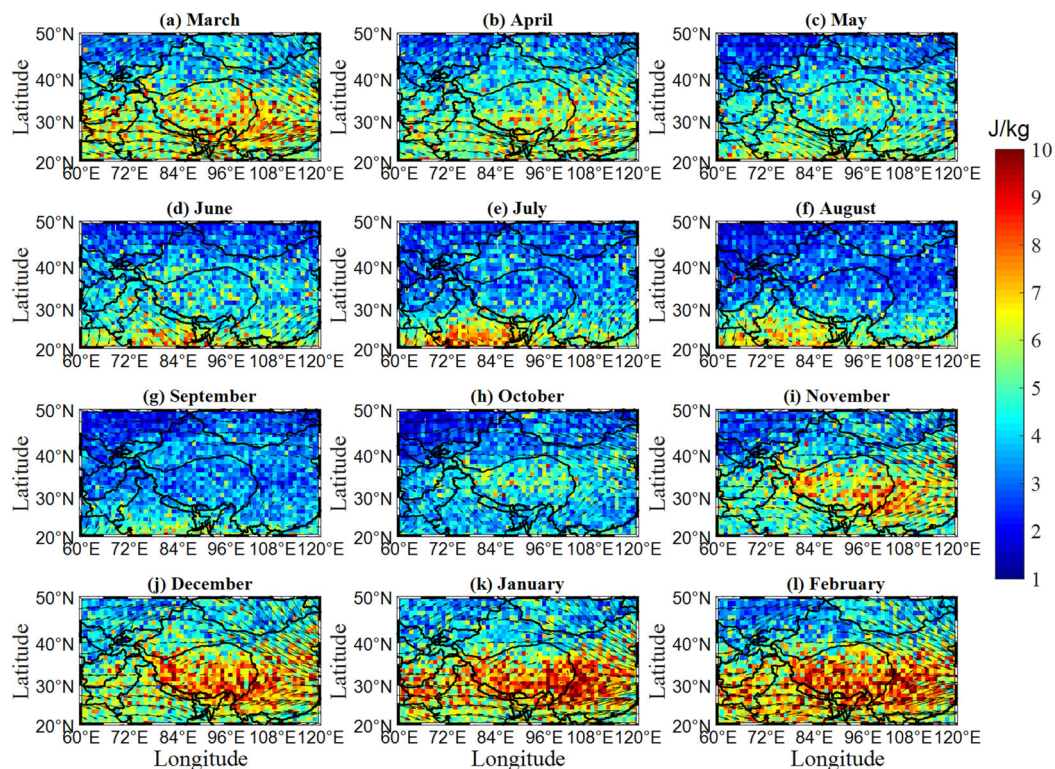


**Figure 7.** The spatial distribution of monthly mean GW Ep of 18–20 km around TP (20–50°N, 60–120°E) from August 2006 to September 2020. Region of TP: Latitude, 25–41°N; longitude: 68–105°E. The arrow represents the background wind.

### 3.3. Correlation between GW Ep and Topography

Topographic waves play a dominant role in GWs around the TP [9]. In order to specifically analyze the relationship between the topography and the GW Ep, this section draws the zonal change and the zonal change rate of the GW Ep and elevation (Figure 8) and the meridional change and the meridional change rate of the GW Ep and elevation (Figure 9) based on the  $2^\circ \times 2^\circ$  monthly mean GWs model, respectively. Table 2 lists the Pearson correlation coefficients between the GW Ep and the elevation for each month corresponding to Figures 8 and 9.

It can be seen from Figure 8 that the zonal topography has a great influence on the zonal GW Ep from October to March with strong background winds (Figure 7). In these months, the changes between the zonal GW Ep and the zonal elevation are highly consistent. With the increase in elevation, the value of the GW Ep becomes larger and reaches the maximum before the maximum elevation (Figure 8a,h–l). The correlation coefficients between the change in the zonal GW Ep and the zonal elevation are 0.673, 0.497, 0.465, 0.405, 0.318, and 0.230, respectively (Table 2). Although the topography has an obvious effect on the zonal GW Ep from November to February, the correlation coefficients are not always larger, such as in February (0.318). In addition, the maximum correlation coefficient (0.673) appears in October (Table 2), but the influence of topography on the zonal GW Ep is not the greatest (Figure 8). Therefore, the magnitude of the correlation coefficient between the elevation and the GW Ep may not clearly indicate the impact of topography on the GW Ep in some months. The change rate between the zonal GW Ep and the zonal elevation shows the same trend from October to March. Near the sharp rise or fall in zonal elevation, the zonal GW Ep also rises or falls sharply (Figure 8m,t–x). The correlation coefficient from October to March is large and the minimum is 0.553 (Table 2). These demonstrate that the

zonal topography has a significant impact on the zonal GW Ep from October to March, and the large elevation or the large topography changes are conducive to promoting GW excitation. Notably, compared with the correlation coefficient between the change in the zonal elevation and the zonal GW Ep, the correlation coefficient between the change rate of the zonal elevation and the zonal GW Ep is larger from November to February when the topography has a strong influence on the GW Ep (Table 2). In particular, the correlation coefficient between the change in the zonal GW Ep and the zonal elevation is too small to represent the large impact of the topography on the GW Ep in February (0.318) and March (0.230) (Table 2). This indicates that the correlation coefficient between the change rate of the GW Ep and the elevation seems to better represent the impact of the topography on the GW Ep. It is worth noting that from November to March, the change/change rate of zonal GW Ep always seems to change earlier than the change/change rate of zonal elevation (Figure 8a,h–l,m,t–x). As can be seen from Figure 7, these are caused by the large GW Ep excited by the strong background wind in the southern part of the TP.

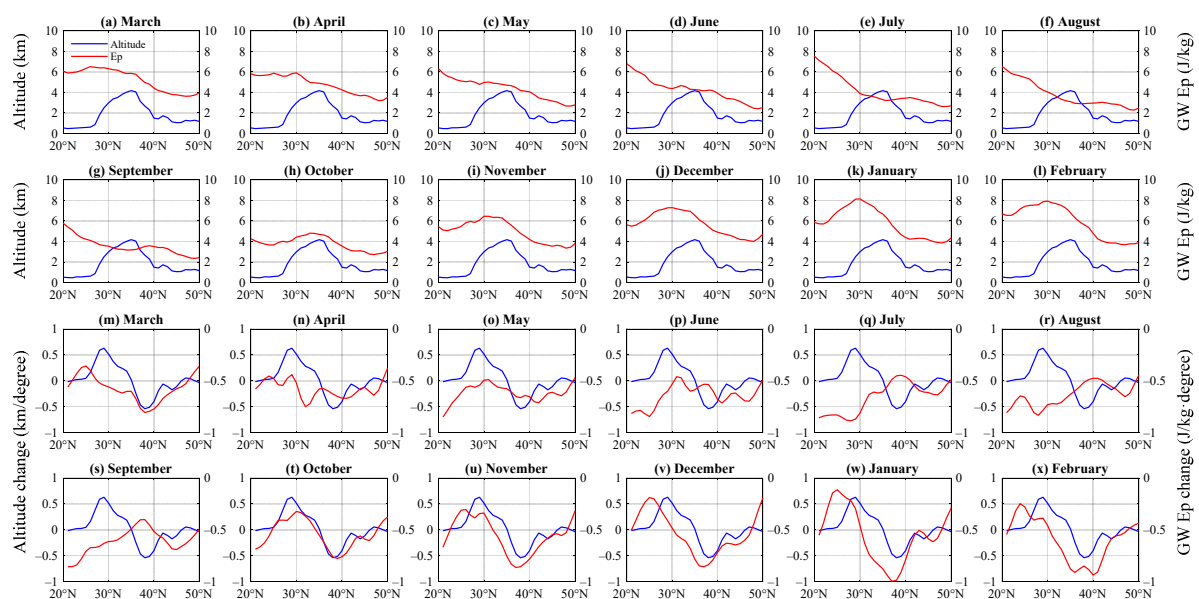


**Figure 8.** The zonal change and zonal change rate of the monthly mean GW Ep and the elevation from August 2006 to September 2020. Latitude from 20 to 50°N, longitude from 68 to 105°E. The red line represents the 18–20 km GW Ep and the blue line represents the elevation.

From April to September, the zonal GW Ep did not change significantly in the region with the large zonal elevation and showed a downward trend with increasing latitude (Figure 8b–g). In addition, the change rate of the zonal GW Ep is negative when the zonal elevation increases sharply (Figure 8n–s). These factors indicate that the weak background wind is not conducive to the excitation of GWs (Figure 7), and these phenomena are related to the poleward propagation of the GW generated by the tropical convection [20,34,36]. Notably, the correlation coefficient between the change/change rate of the zonal GW Ep and the zonal elevation was mainly negative from April to September, and the maximum negative correlation coefficient between the change in the zonal GW Ep and the zonal elevation was  $-0.494$  in July, which may be caused by the fact that the elevation increases and the GW Ep decreases with the increase in latitude in the 20–35°N latitude zone (Figure 8e). Furthermore, the maximum negative correlation coefficient between the change rate of the zonal GW Ep and the zonal elevation was  $-0.778$  in August (Table 2), which is because the change rate of the elevation and the GW Ep showed an opposite trend (Figure 8r). Above all, the zonal topographic influence on the zonal GW Ep was small from April to September.

Figure 9 shows the meridional change and the meridional change rate of the GW Ep and the elevation. The GW Ep in Figure 9a–l shows the same periodicity as Figure 7 with the maximum from November to March and the minimum from July to September,

which may be related to the periodic changes in the background wind. From November to February, the meridional topography has a significant effect on the meridional GW Ep, and the value of meridional GW Ep is large when the area has a high meridional elevation (Figure 9i–l). From Table 2, the correlation coefficients between the change/change rate of the meridional GW Ep and the meridional elevation were large from November to February, except for January (0.305/0.223). In addition, the maximum correlation coefficient between the change in the meridional GW Ep and the meridional elevation appears in October (0.835) when the effect of the meridional topography on the meridional GW Ep is not obvious. This proves, once again, that the magnitude of the correlation coefficient between the elevation and the GW Ep may not clearly indicate the impact of topography on the GW Ep in some months. From Figure 9u–x, within the longitude range of 73–86°E where the meridional elevation changes sharply, the meridional GW Ep also shows the same trend with correlation coefficients of 0.95, 0.96, 0.81, and 0.80, respectively. These demonstrated that large topographic changes are conducive to the generation of GWs, and the GWs in the 73–86°E longitude zone of the TP are strongly excited by the topography and the strong background wind (Figure 7). Furthermore, the excited GWs may be influenced by the strong zonal winds and propagate upward into the lower stratosphere. In addition, it was found that the change/change rate of the meridional GW Ep from November to February also showed significant changes from 95–105°E, which was caused by the maximum of GW Ep in the southeast of TP (Figure 7).

From April to September, the meridional GW Ep is affected by the weak background wind (Figure 7) with a value of less than 2 J/kg and does not show obvious change with the meridional elevation (Figure 9b–g), and the change rate of the meridional GW Ep fluctuated around 0 (Figure 9n–s). However, the correlation coefficient between the change in the meridional GW Ep and the meridional elevation is larger in May (0.548) and September (0.583) (Table 2). This phenomenon does not correspond to that in Figure 9c,g, which indicates the change in the meridional GW Ep is only slightly affected by the meridional elevation. From Table 2, the correlation coefficients between the change rate of the meridional GW Ep and the meridional elevation are small, which shows, once again, that the correlation coefficient between the change rate of the GW Ep and the elevation better represents the impact of the topography on the GW Ep. These indicate that the meridional topography has little influence on the meridional GW Ep from April to September.

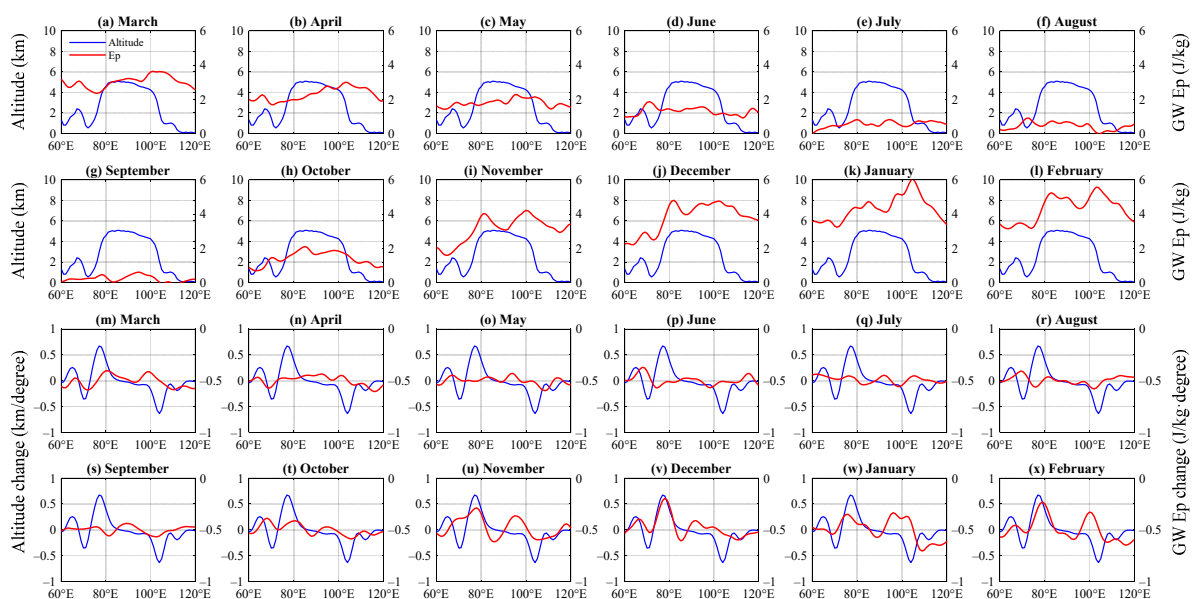


**Figure 9.** The meridional change and the meridional change rate of monthly mean GW Ep and the elevation from August 2006 to September 2020. Latitude from 30 to 35°N, longitude from 60 to 120°E. The red line represents the 18–20 km GW Ep and the blue line represents the elevation.

**Table 2.** The Pearson correlation coefficient between the GW Ep and the elevation from August 2006 to September 2020. The correlation coefficients that pass the 95% significance test are in bold.

Time (Month)	Zonal		Meridional	
	Change	Rate of Change	Change	Rate of Change
March	0.230	<b>0.538</b>	<b>0.245</b>	<b>0.264</b>
April	0.062	0.271	0.162	0.222
May	0.060	<b>0.490</b>	<b>0.548</b>	0.177
June	−0.136	0.043	<b>0.290</b>	−0.113
July	<b>−0.494</b>	<b>−0.728</b>	0.152	0.147
August	<b>−0.442</b>	<b>−0.778</b>	<b>0.384</b>	−0.044
September	<b>−0.376</b>	<b>−0.396</b>	<b>0.583</b>	<b>0.281</b>
October	<b>0.673</b>	<b>0.847</b>	<b>0.835</b>	<b>0.539</b>
November	<b>0.497</b>	<b>0.760</b>	<b>0.480</b>	<b>0.519</b>
December	<b>0.465</b>	<b>0.553</b>	<b>0.536</b>	<b>0.737</b>
January	<b>0.405</b>	<b>0.553</b>	<b>0.305</b>	<b>0.223</b>
February	0.318	<b>0.608</b>	<b>0.512</b>	<b>0.457</b>

### 3.4. Periodic Variation of the GW Ep in the Lower Stratosphere

The GW Ep in the lower stratosphere of the TP show periodic changes (Figures 8 and 9). In the area with strong background wind and large topography, the GW Ep is larger and has obvious periodic changes. In order to specifically analyze the reasons for the periodicity of the GW Ep in the lower stratosphere of the TP, as shown in Figure 10, seven typical regions are selected in this section. Regions #1 and #2 represent the regions with weak background wind and strong background wind, respectively. From Figure 10, Region #3 is selected due to its special topography with weak background wind due to being blocked by the surrounding topography, and the elevation of the southern topography of Region #3 is large. Regions #4 and #5 represent the regions of the small GW Ep and the large GW Ep, respectively. Regions #6 and #7 represent the regions of the small topography and the large topography, respectively. The specific ranges of these regions are shown in Table 3.

The GWs in the lower stratosphere of TP mainly come from the upward propagation of the topographic waves generated by the interaction between the background wind and topography. Therefore, the periodic variation of the GW Ep in the lower stratosphere may be related to the periodic background winds that were blocked by the topography to generate the topographic wave and then propagated upward into the lower stratosphere. In addition, the correlation coefficient between the GW Ep and the background wind was influenced by the proportion of topographic waves in GWs. Figure 11 shows the monthly mean time series of the background wind, the zonal wind, and the GW Ep for each region, and the correlation coefficients between the GW Ep and the background wind and the correlation coefficients between the GW Ep and the zonal wind in each region are shown in Table 3. From Figure 11a,b, although the zonal wind in Region #1 is stronger than that in Region #2, a large GW Ep occurs in Region #2 with strong background wind and the small GW Ep in Region #1 corresponds to the weak background wind. The correlation coefficient between the GW Ep and the background wind in Region #1 (Region #2) is larger than the correlation coefficient between the GW Ep and the zonal wind (Table 3), indicating that the periodicity of the GW Ep in the lower stratosphere is greatly affected by background wind in Regions #1 and #2. Furthermore, the correlation coefficients between the GW Ep and the background wind in Regions #1 and #2 are 0.422 and 0.621, respectively. This indicates that the GW Ep excited by strong background wind propagates upward to the lower stratosphere, therefore, the correlation between the GW Ep and the background wind in Region #2 is stronger than that in Region #1. Notably, the background wind is weak in Region #3 (Figure 11c) but the correlation coefficient between the GW Ep and the background wind is greater than that in Region #2. On the one hand, the GWs also have horizontal propagation in the process of upward propagation, and Region #3 is near the larger GW Ep. On the other hand, Region #3 is close to the edge of the TP with

large topographic changes, which is conducive to the excitation of GWs (Figure 7). From Table 3, we can observe the zonal wind in Region #4 is stronger than that in Region #5 (Figure 11), and the large correlation coefficient between the GW Ep and the background wind and the large correlation coefficient between the GW Ep and the zonal wind both appear in Region #5 with the large GW Ep (Figure 11d,e). This indicates that the GW Ep in the lower stratosphere is mainly affected by the background wind in Regions #4 and #5, and the proportion of topographic waves in Region #5 excited by the interaction between the background wind and the topography is larger in GWs. The intensity of the background wind in Regions #6 and #7 is similar (Figure 11f,g), and the elevation of Region #7 is larger (Figure 10), indicating the stronger excitation between the background wind and the larger topography in Region #7 to generate the GWs. However, the correlation coefficient between the GW Ep and the background wind in Region #7 (0.822) is smaller than that in Region #6 (0.828). In addition, the correlation coefficient between the GW Ep and the zonal wind (0.838) is larger than the correlation coefficient between the GW Ep and background wind (0.828) in Region #6. These results indicate that the GW Ep in Region #6 is strongly influenced by the zonal wind during its upward propagation, which promotes the topographic waves to reach the lower stratosphere.

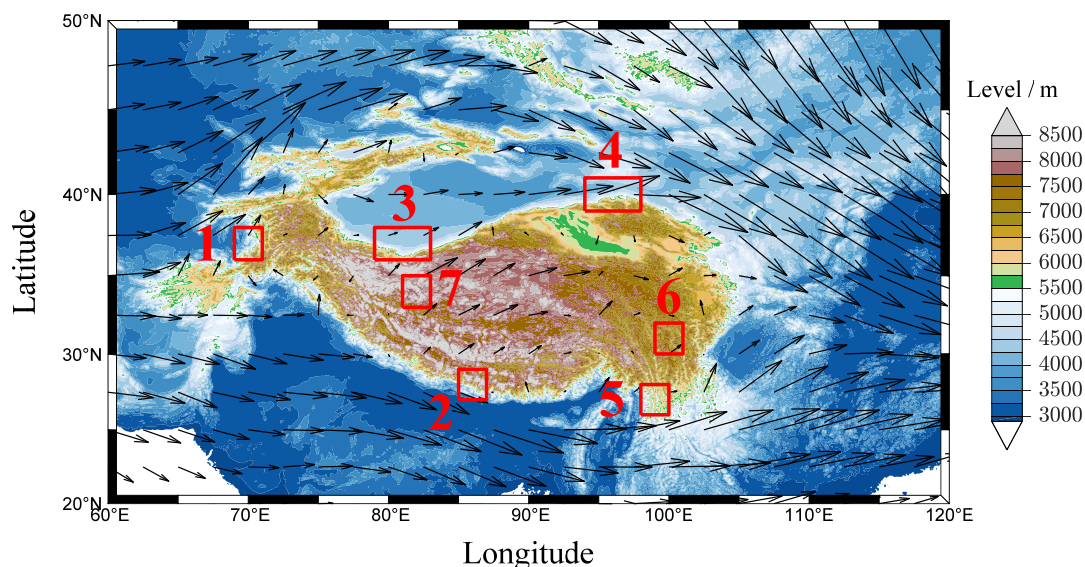


**Figure 10.** The selected region. The arrow represents the background wind vector of 3 km.

**Table 3.** Region selection and Pearson correlation coefficient between the GW Ep and the background wind/the zonal wind in each region. The correlation coefficient in bold indicates that it passes the 95% significance test.

Region	Regional Scope	Characteristic	Correlation Coefficient	
			GW Ep and Background Wind	GW Ep and Zonal Wind
1	Latitude: 36–38°N Longitude: 69–71°E	Weak background wind	<b>0.422</b>	<b>0.315</b>
2	Latitude: 27–29°N Longitude: 85–87°E	Strong background wind	<b>0.621</b>	<b>0.605</b>
3	Latitude: 36–38°N Longitude: 79–83°E	Weak background wind	<b>0.766</b>	<b>0.737</b>
4	Latitude: 39–41°N Longitude: 94–98°E	Small GW Ep	<b>0.575</b>	<b>0.563</b>
5	Latitude: 26–28°N Longitude: 98–100°E	Large GW Ep	<b>0.774</b>	<b>0.736</b>

Table 3. Cont.

Region	Regional Scope	Characteristic	Correlation Coefficient	
			GW Ep and Background Wind	GW Ep and Zonal Wind
6	Latitude: 30–32°N Longitude: 99–101°E	Low topography	0.828	0.838
7	Latitude: 33–35°N Longitude: 81–83°E	High topography	0.822	0.782

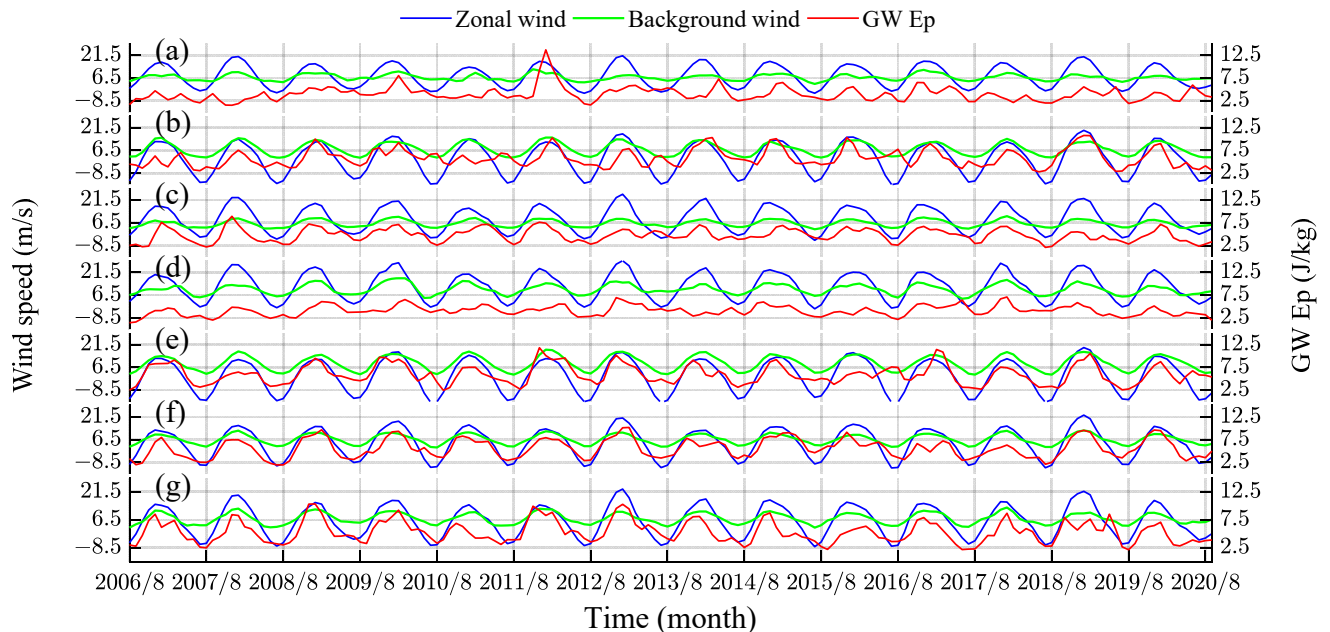


**Figure 11.** The relationship between the GW Ep over different regions depicted in Table 3 with the background wind and the zonal wind from August 2006 to September 2020. (a) Region #1; (b) Region #2; (c) Region #3; (d) Region #4; (e) Region #5; (f) Region #6; (g) Region #7. The background wind is the average over the elevation range of each region. Blue solid line, zonal wind; green solid line, background wind; red solid line, GW Ep.

### 3.5. Relationship between GW Ep and Background Wind and Zonal Wind

The main mechanism of GW generation around the TP is the blocking of background wind by topography, and the GWs are affected by the zonal wind during its upward propagation [35,37]. Therefore, the differences in topography, background wind, and zonal wind are important factors for the spatial distribution of the GWs in the lower stratosphere. In order to analyze the specific reasons for the spatial distribution of the GW Ep in the lower stratosphere around the TP, this paper presents the time series of the background wind, the zonal wind, and the GW Ep in Figure 12 for each region based on the  $2^\circ \times 2^\circ$  monthly mean GW model.

The background wind and the zonal wind have similar periodicity in each region, which is strong around February and weak around August. The GW Ep of each region is obviously different due to the influence of the different background wind and the different zonal wind, but it shows the same periodic change as the background wind and the zonal wind in its region. For example, the background wind and the zonal wind in Region #7 are significantly stronger than that in Region #1 around February when the background wind and the zonal wind are strong, and the background wind and the zonal winds in Region #7 are weaker than those in Region #1 around August when the background wind and the zonal wind are weak. Therefore, the GW Ep of Regions #1 and #7 is also larger around February and smaller around August. Around February, the value of the GW Ep in Region

#7 is significantly larger than that in Region #1 on the whole and the value of the GW Ep in Region #7 is smaller than that in Region #1 around August. These results show that the large GW Ep in the lower stratosphere of the TP is related to the strong background wind and the strong zonal wind.

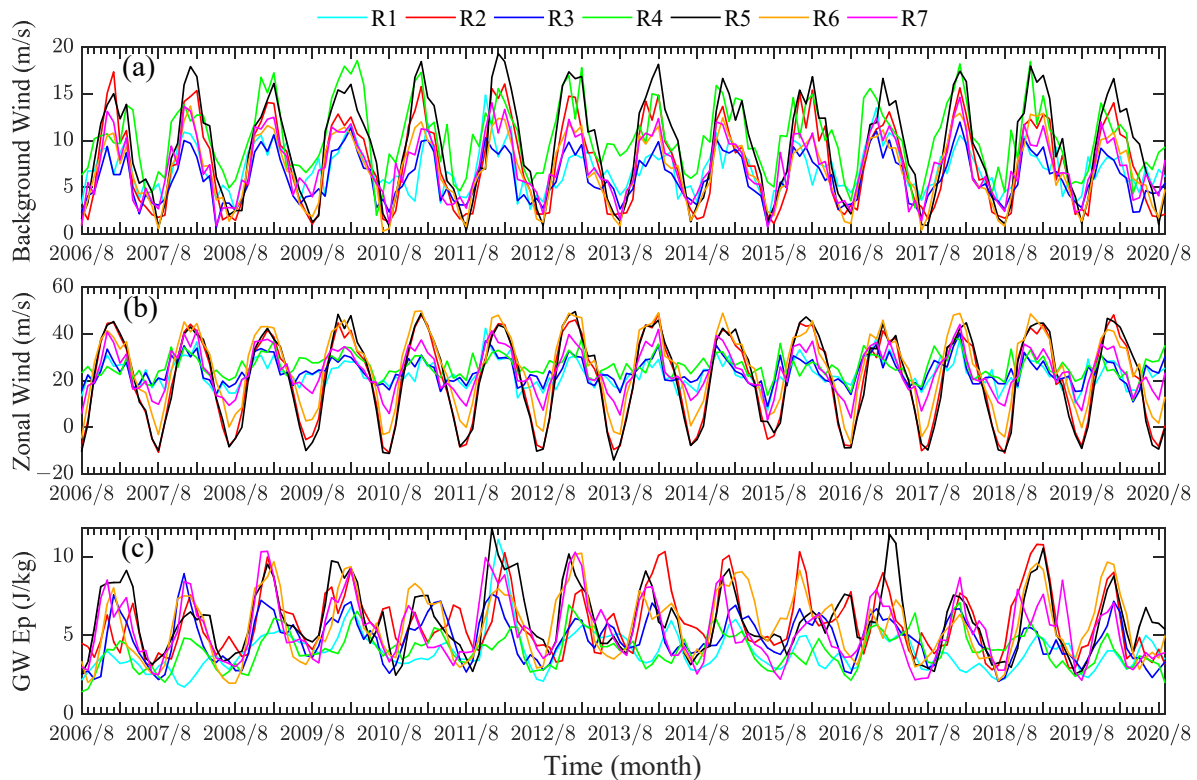


**Figure 12.** The time series of (a) the background wind, (b) the zonal wind (8–18 km), and (c) the GW Ep (18–20 km) in each region from August 2006 to September 2020. The background wind is the average value of the background wind within the elevation range of each region. The solid lines in cyan, red, blue, green, black, orange, and magenta represent the variables from Region #1 to Region #7, respectively.

The background wind in Regions #1 and #3 due to being blocked by the surrounding topography leads to significantly weaker wind than that in Region #2 around February when the background wind is strong. In addition, the zonal winds in Region #2 are also significantly stronger than those in Regions #1 and #3 around February. This suggests that around February, not only is the excitation of GWs stronger in Region #2 but the excited GWs are also more conducive to upward propagation. Therefore, the GW Ep of Region #2 in Figure 12c is larger than that of Regions #1 and #3 on the whole around February. It is worth noting that the magnitude of the background wind and the zonal wind are similar in Regions #1 and #3, but the GW Ep of Region #3 is larger than that of Region #1 as a whole, which may be due to the horizontal spread of the large GW Ep near Regions #2. Around August, the zonal winds in Region #2 are weak easterly winds, indicating that the quasi-static GWs caused by the topography have been filtered by the zero wind speed, but the value of GW Ep is greater than that in Regions #1 and #3. As can be seen from Figure 7, this may be due to the spread of the GW Ep generated by tropical convection to Region #5.

The background winds in Regions #4 and #5 are similar and strong around February, so the reason the value of the GW Ep in Region #5 is larger than that in Region #4 around February is that the zonal winds in the upward propagation of the GW Ep in Region #5 are stronger than that in Region #4, which explains that the larger GW Ep in the southeast of TP in winter is caused by the strong background wind and the strong zonal wind. The background wind and the zonal wind in Region #5 are weaker than those in Region #4

around August, and the zonal wind in Region #5 is easterly, but the value of the GW Ep in Region #5 is similar to Region #4, which may also be attributed to the GW Ep generated by tropical convection.

The strength of the background wind is similar in Regions #6 and #7 (Figure 12a), but the topography of Region #7 is larger (Figure 9), which indicates that Region #7 is more conducive to the generation of GW Ep. The zonal wind in Region #6 is stronger than that in Region #7 around February (Figure 12b), indicating that the GW Ep in Region #6 is favorable for upward propagation around February, which again proves that the GW Ep in Region #6 mentioned in Section 3.4 is affected by the strong zonal winds in its upward propagation. Therefore, it can be found from Figure 12c that around February, when the zonal wind of Region #7 is significantly weaker than that of Region #6, the GW Ep in Region #6 is larger (2011, 2015, 2016, and 2019). When the zonal wind of Region #7 approaches Region #6, the GW Ep is larger in Region #7 (2007–2009, 2012, 2014, 2017, and 2018). This indicates that the GW Ep in the lower stratosphere is influenced by the background wind and the topography at excitation and the zonal wind during upward propagation. It is worth noting that around August, the values of the GW Ep in Regions #6 and #7 are similar, and the values of background wind are also similar. This suggests that in Regions #6 and #7 when the background wind is weak and not conducive to GW excitation, the zonal wind has little influence on the upward propagation of the GWs and the GW Ep in the lower stratosphere is mainly affected by the background wind.

### 3.6. Reconstruction of GW Ep in Lower Stratosphere

The GWs' activity in the lower stratosphere around the TP is mainly influenced by the background wind at excitation and the zonal wind during upward propagation (Figure 12). In order to quantitatively analyze the influence of the background wind and zonal wind on the GW Ep, a multivariable linear regression model [39,40] was adopted to reconstruct the GW Ep of the TP in the lower stratosphere. The formula is as follows:

$$y(t) = a_0 + a_1 \cdot t + a_2 \cdot \text{Background\_wind}(t) + a_3 \cdot \text{U\_wind}(t) \quad (6)$$

where  $y$  is the time series of the GW Ep (18~20 km) on the TP,  $a_0$  is the constant term of the model,  $a_1$  is the trend term, and  $a_2$  and  $a_3$  are the coefficients of the background wind and the zonal wind, respectively. *Background\_wind* and *U\_wind* represent the time series of the background wind and the zonal wind over the TP, respectively. The background wind is the average value of the background wind over the elevation range of TP (3–8 km), and the zonal wind is the average value of the zonal wind over the elevation range from TP to the lower stratosphere (8~18 km).

The  $p$ -value of the F-test in this model is  $8.03 \times 10^{-60}$  and the goodness of fit is 0.811, indicating that the model fit is effective and 81.1% of the GW Ep of TP in the lower stratosphere can be determined by this model. Figure 13 shows the fitting curve and the corresponding residuals of the model. The true value is essentially on or near the fitted curve and the corresponding residual fluctuates around 0, which indicates that the model is well fitted. The coefficients of the fitted curves were 2.14, 0.0023, 0.607, and  $-0.139$ , respectively, denoting that the GW Ep in the lower stratosphere over the TP shows an increasing trend of 0.0023 J/kg per month, and the influence of background wind on the GW Ep in the lower stratosphere is greater than that of the zonal wind. Energy dissipation occurs in the upward propagation of the GWs. This process is mainly affected by the zonal winds, and the strong zonal westerly winds will reduce energy dissipation in this process [37]. Therefore, the negative correlation coefficient of zonal wind indicates the influence of the energy attenuation of the GWs during upward propagation on the GW Ep in the lower stratosphere.

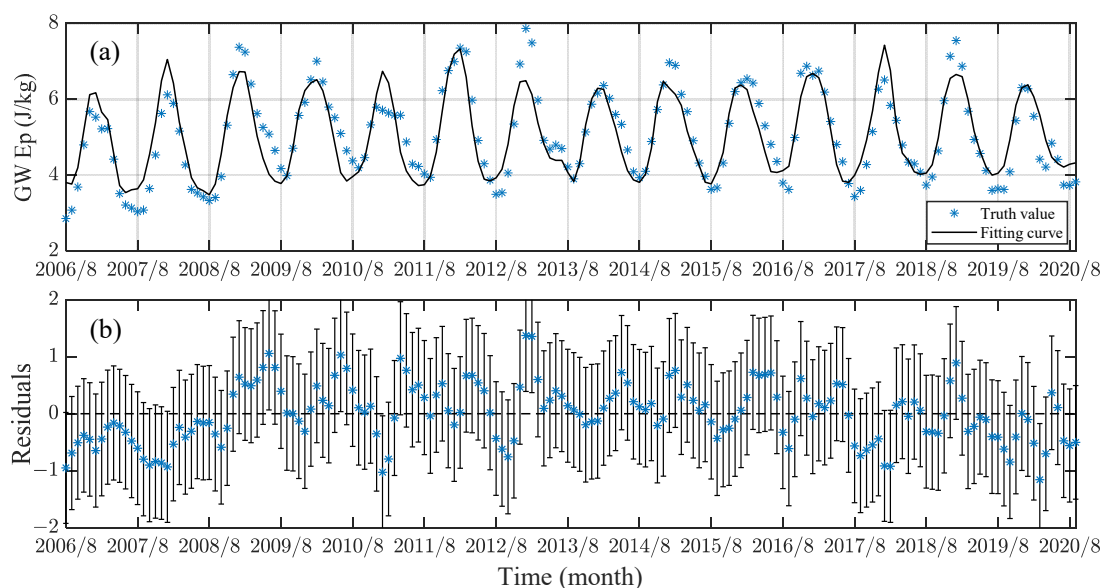


**Figure 13.** The GW Ep fitting curves (a) and the corresponding residuals (b) of multivariable linear regression model in the lower stratosphere over TP (25–41°N, 68–105°E) from August 2006 to September 2020.

### 3.7. General Process of Topography Wave Excitation and Propagation

Based on the above analysis, we can know that the GWs in the TP are generated by the interaction between the topography and the background wind and are then propagated upward to the lower stratosphere under the influence of the zonal wind. Zeng et al. [9] pointed out that the existence of the topographic waves can be proven by the spatial distribution of the GW Ep (Figure 7), the relationship between the GW Ep and the topography (Figures 8 and 9), and the obvious filtering by the zero-speed wind as it propagates upward (Figure 6). The obvious filtering of the GW Ep by the zero-speed wind and the high correlation between the distribution of the GW Ep and the topography indicate that topographic waves play a dominant role over the TP in the lower stratosphere. Figure 14 shows the general process of the excitation and propagation of topographic waves around the TP. Firstly, the mountain blocks the background wind to excite the GWs (topographic waves) (Figure 14a). The strong background wind and the large elevation or the large topography changes will intensely motivate GWs, especially in the southeast of the TP. Then, the motivated GWs propagate upward (Figure 14b). The GWs will dissipate energy during upward propagation, which is affected by the zonal wind. The strong westerly wind reduces the energy dissipation in this process and promotes the GWs to propagate upward to the middle and upper atmosphere. The westerly wind with a stronger wind speed will promote the GWs to propagate upward. When the west wind turns into the east wind, the zero-speed wind will filter the quasi-static GWs motivated by the topography, and the GWs decrease sharply above the zero-speed wind. Then, the reduced GWs continue to propagate upward under the east wind.

In this section, we provide an example to describe the specific process of the GWs' excitation when the background wind is blocked by the TP and the upward propagation of GWs around the TP. The spatial distribution of the topography of TP, the background wind (3 km), the zonal wind (8–18 km), and the GW Ep (18–20 km) was drawn based on the annual average of the observed data in March (Figure 14c–f). There are strong background winds and large topographic changes in the southern part of the TP (Figure 14c,d). The strong background wind is blocked by the topography, which promotes the excitation of GWs. The strong zonal westerly winds in the southeastern part of the TP (25–30°N, 95–105°E) promote the upward propagation of GWs (Figure 14e), which makes the GW Ep largest in the lower stratosphere in this region (Figure 14f). In contrast, the GW Ep is relatively small in the northwestern plateau (35–40°N, 75–86°E). The background wind in

this area is weak due to being blocked by the high surrounding topography (Figure 14c,d), which is not conducive to GWs' excitation. In addition, the zonal winds in the upward propagation of GWs are weak (Figure 14e). Thus, the GW Ep reaching the lower stratosphere in this region is small (Figure 14f).

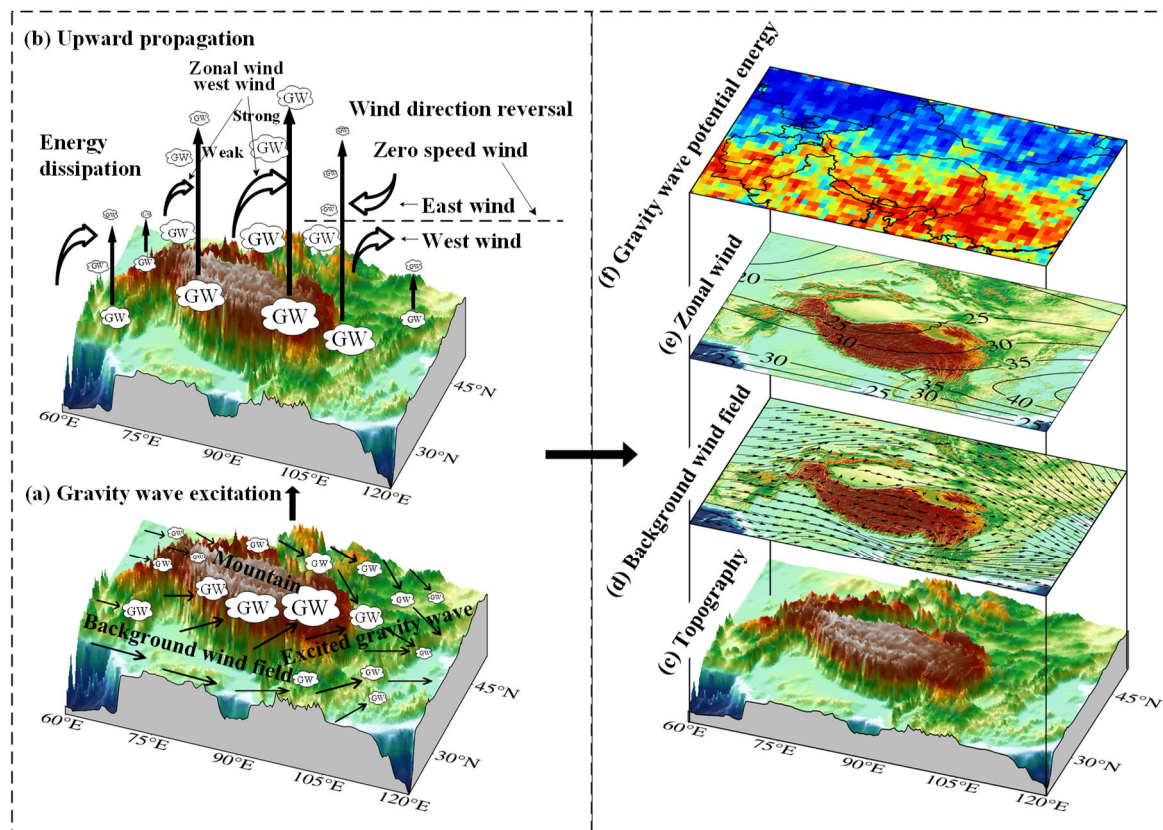


**Figure 14.** The general process of (a) the GW (topographic waves) excitation and (b) the upward propagation around TP, and the corresponding observations of (c) the topography, (d) the background wind at the altitude of 3 km, (e) the average zonal wind of 8–18 km, and (f) the GW Ep in the lower stratosphere (18–20 km).

#### 4. Conclusions

In this paper, a  $2^\circ \times 2^\circ$  monthly mean GWs model around the TP for 14 years from August 2006 to September 2020 was established based on the dry temperature profiles of four GNSS RO missions: COSMIC, METOP-A, METOP-B, and METOP-C. The stability of the dry temperature observation of each RO mission and the bias between the dry temperature of each RO mission and the combined mean temperature of the four GNSS RO missions from August 2006 to September 2020 were analyzed. It was proved that the dry temperature observation of each RO mission has good stability, and the combination of dry temperature observations by each RO mission is available and can be used for high-precision GW Ep extraction. The vertical distribution of GWs over the TP and the spatial distribution of GWs around the TP were analyzed. The effect of topography on the GW Ep in the lower stratosphere was investigated. Then the periodic variation of the GW Ep over the TP and the influence of the background winds during excitation and the zonal winds during upward propagation on the GW Ep in the lower stratosphere were explored in seven typical regions. The multivariable linear regression models were then used to reconstruct the GW Ep of the lower stratosphere over the TP based on the background wind and the zonal wind. Finally, the general process of topographic wave excitation and upward propagation around the TP was summarized. This paper draws the following conclusions.

The GW Ep in the lower stratosphere of the TP has obvious periodic changes. Around February, the zonal winds are strong westerlies and the value of the GW Ep is large. Around August, the zonal wind changes from westerly to easterly and the zero-speed wind filters the quasi-static GWs, so the value of the GW Ep in the lower stratosphere is small. The spatial distribution of the GW Ep in the lower stratosphere is highly correlated with the spatial distribution of the background wind and the topography around the TP. The GW Ep is large when the background winds are strong from November to March and the GW Ep is small when the background winds are weaker from July to September. Furthermore, there is a large GW Ep at the edge of the TP, which mainly exists in the southeast of the TP where the background wind is strong.

The GW Ep in the lower stratosphere over the TP is mainly the topographic waves generated by the interaction between the topography and the background wind, which then propagate upward to the lower stratosphere under the influence of the zonal wind. The interaction between the strong background wind (November–February) and large elevation or large topographic changes strongly excite the GWs, and the strong zonal wind reduces the energy dissipation of GWs propagating upward and promotes GWs to propagate to the lower stratosphere. When the background wind and the zonal wind are strong around February, the value of GW Ep in the lower stratosphere of the TP is large in the region with strong background wind and strong zonal wind. In order to quantitatively analyze the influence of the background wind and zonal wind on the GW Ep, a multivariable linear regression model was adopted to reconstruct the GW Ep of the TP in the lower stratosphere. The results show that the model has a good fitting result, and 81.1% of the GW Ep can be determined by the model. These indicated that the GW Ep was dominated by the topographic wave over TP, and the background wind has a greater influence on the GWs than the zonal wind. The periodic variation of the GW Ep in the lower stratosphere is mainly affected by the periodic background winds, and this effect is larger in the region where the background wind and the topography strongly excited the topographic waves.

Based on the  $2^{\circ} \times 2^{\circ}$  monthly mean GWs model, this paper confirms that the GWs in the TP are dominated by the topographic waves generated by the interaction between the topography and the background wind. Furthermore, the strong background wind and the large elevation or the large topography changes intensely motivate GWs (topographic waves), and the strong westerly wind promotes the GWs to propagate upward to the middle and upper atmospheres. These are helpful to deepen the understanding of GWs of the TP and are of great significance to GW parameterization in the relevant models. In addition, this paper uses the combination of four RO missions (COSMIC, METOP-A, METOP-B, and METOP-C) to extend the research time and increase the resolution of the results, which provides a good basis for subsequent research of GWs with high precision and a long time scale.

**Author Contributions:** Conceptualization, Z.C.; methodology, Z.C. and Y.G.; software, Z.C. and Y.G.; validation, L.L.; formal analysis, Y.G. and L.L.; investigation, Y.G.; resources, Z.C.; data curation, Y.G., W.Y. and H.L.; writing—original draft preparation, Z.C. and Y.G.; writing—review and editing, Z.C. and X.H.; visualization, Z.C.; supervision, Z.C., X.H., X.G. and K.L.; project administration, Z.C. and K.L.; funding acquisition, Z.C., X.H., X.G. and K.L. All authors have read and agreed to the published version of the manuscript.

**Funding:** This research was funded by the National Natural Science Foundation of China (Grants No. 41904031, No. 42061077, No. 41904002, No. 42104023, and No. 42101457), the Jiangxi Provincial Natural Science Foundation (Grants No. 20202BABL213033), the State Key Laboratory of Geodesy and Earth's Dynamics (Grants No. SKLGED2021-2-2), the Key Laboratory for Digital Land and Resources of Jiangxi Province, East China University of Technology (Grants No. DLLJ201905), the 2022 Science and Technology Think Tank Young Talent Program (20220615ZZ07110308), the PhD early development program of East China University of Technology (Grants No. DHBK2018006), and the Jiangxi Provincial Graduate Innovation Fund Project (YC2021-S615).

**Data Availability Statement:** The GNSS RO observations of COSMIC, METOP-A, METOP-B, and METOP-C were obtained from <https://data.cosmic.ucar.edu/gnss-ro/> (last accessed on 16 July 2022). The zonal wind data and the meridional wind data are provided by ERA5 at <https://cds.climate.copernicus.eu/cdsapp#!/dataset/> (last accessed on 16 July 2022).

**Acknowledgments:** We acknowledge the CDAAC for the use of the GNSS-RO datasets. We are grateful to ERA5 for the zonal wind and meridional wind datasets. We also thank the anonymous reviewers for their role in improving the manuscript.

**Conflicts of Interest:** The authors declare no conflict of interest.

## References

1. Lindzen, R.S. Turbulence and stress owing to gravity wave and tidal breakdown. *J. Geophys. Res. Ocean.* **1981**, *86*, 9707–9714. [[CrossRef](#)]
2. Holton, J.R. The role of gravity wave induced drag and diffusion in the momentum budget of the mesosphere. *J. Atmos. Sci.* **1982**, *39*, 791–799. [[CrossRef](#)]
3. Holton, J.R. The influence of gravity wave breaking on the general circulation of the middle atmosphere. *J. Atmos. Sci.* **1983**, *40*, 2497–2507. [[CrossRef](#)]
4. Garcia, R.R.; Solomon, S. The effect of breaking gravity waves on the dynamics and chemical composition of the mesosphere and lower thermosphere. *J. Geophys. Res. Atmos.* **1985**, *90*, 3850–3868. [[CrossRef](#)]
5. Fritts, D.C.; Nastrom, G.D. Sources of mesoscale variability of gravity waves. Part II: Frontal, convective, and jet stream excitation. *J. Atmos. Sci.* **1992**, *49*, 111–127. [[CrossRef](#)]
6. Alexander, M.J.; Vincent, R.A. Gravity waves in the tropical lower stratosphere: A model study of seasonal and interannual variability. *J. Geophys. Res. Atmos.* **2000**, *105*, 17983–17993. [[CrossRef](#)]
7. Fritts, D.C.; Alexander, M.J. Gravity wave dynamics and effects in the middle atmosphere. *Rev. Geophys.* **2003**, *41*, 1003. [[CrossRef](#)]
8. Hoffmann, L.; Xue, X.; Alexander, M.J. A global view of stratospheric gravity wave hotspots located with Atmospheric Infrared Sounder observations. *J. Geophys. Res. Atmos.* **2013**, *118*, 416–434. [[CrossRef](#)]
9. Zeng, X.Y.; Xue, X.H.; Dou, X.K.; Liang, C.; Jia, M.J. COSMIC GPS observations of topographic gravity waves in the stratosphere around the Tibetan Plateau. *Sci. China Earth Sci.* **2017**, *60*, 188–197. [[CrossRef](#)]
10. Medvedev, A.S.; Klaassen, G.P. Parameterization of gravity wave momentum deposition based on nonlinear wave interactions: Basic formulation and sensitivity tests. *J. Atmos. Sol.-Terr. Phys.* **2000**, *62*, 1015–1033. [[CrossRef](#)]
11. Cai, X.; Yuan, T.; Liu, H.L. Large-scale gravity wave perturbations in the mesopause region above Northern Hemisphere midlatitudes during autumnal equinox: A joint study by the USU Na lidar and Whole Atmosphere Community Climate Model. *Ann. Geophys.* **2017**, *35*, 181–188. [[CrossRef](#)]
12. Yang, S.S.; Pan, C.J.; Das, U. Investigating the Spatio-Temporal Distribution of Gravity Wave Potential Energy over the Equatorial Region Using the ERA5 Reanalysis Data. *Atmosphere* **2021**, *12*, 311. [[CrossRef](#)]
13. Baumgarten, K.; Gerding, M.; Baumgarten, G.; Lübken, F.-J. Temporal variability of tidal and gravity waves during a record long 10-day continuous lidar sounding. *Atmos. Chem. Phys.* **2018**, *18*, 371–384. [[CrossRef](#)]
14. Xu, X.H.; Guo, J.C.; Luo, J. Analysis of the active characteristics of stratosphere gravity waves over the Qinghai-Tibetan Plateau using COSMIC radio occultation data. *Chin. J. Geophys.* **2016**, *59*, 1199–1210. (In Chinese) [[CrossRef](#)]
15. Wei, D.; Tian, W.S.; Chen, Z.Y.; Zhang, J.K.; Xu, P.P.; Huang, Q.; Wei, Y.Y.; Zhang, J. Upward transport of air mass during a generation of orographic waves in the UTLS over the Tibetan Plateau. *Chin. J. Geophys.* **2016**, *59*, 791–802. (In Chinese) [[CrossRef](#)]
16. Wang, L.; Alexander, M.J. Global estimates of gravity wave parameters from GPS radio occultation temperature data. *J. Geophys. Res. Atmos.* **2010**, *115*, D21122. [[CrossRef](#)]
17. Xu, X.H.; Guo, J.C.; Luo, J. Analysis of the Global Distribution of the Atmospheric Gravity Wave Parameters Using COSMIC Radio Occultation Data. *Geomat. Inf. Sci. Wuhan Univ.* **2015**, *40*, 1493–1498. [[CrossRef](#)]
18. Kursinski, E.R.; Hajj, G.A.; Schofield, J.T.; Linfield, R.P.; Hardy, K.R. Observing Earth's atmosphere with radio occultation measurements using the Global Positioning System. *J. Geophys. Res. Atmos.* **1997**, *102*, 23429–23465. [[CrossRef](#)]
19. Hei, H.; Tsuda, T.; Hirooka, T. Characteristics of atmospheric gravity wave activity in the polar regions revealed by GPS radio occultation data with CHAMP. *J. Geophys. Res.* **2008**, *113*, D04107. [[CrossRef](#)]
20. Liang, C.; Xu, X.H.; Chen, T.D. An investigation of the global morphology of stratosphere gravity waves based on COSMIC observations. *Chin. J. Geophys.* **2014**, *57*, 3668–3678. (In Chinese) [[CrossRef](#)]
21. Khan, A.; Jin, S.G. Effect of gravity waves on the tropopause temperature, height and water vapor in Tibet from COSMIC GPS Radio Occultation observations. *J. Atmos. Sol.-Terr. Phys.* **2016**, *138*, 23–31. [[CrossRef](#)]
22. Luo, J.; Chen, Z.P.; Xu, X.H. Specific humidity response in the troposphere and lower stratosphere to ONI revealed by COS-MIC observations. *Chin. J. Geophys.* **2018**, *61*, 466–476. (In Chinese) [[CrossRef](#)]
23. Chen, Z.P.; Li, J.C.; Luo, J.; Cao, X.Y. A New Strategy for Extracting ENSO Related Signals in the Troposphere and Lower Stratosphere from GNSS RO Specific Humidity Observations. *Remote Sens.* **2018**, *10*, 503. [[CrossRef](#)]
24. Horinouchi, T.; Tsuda, T. Spatial structures and statistics of atmospheric gravity waves derived using a heuristic vertical cross-section extraction from COSMIC GPS radio occultation data. *J. Geophys. Res.* **2009**, *114*, D16110. [[CrossRef](#)]

25. Hindley, N.P.; Wright, C.J.; Smith, N.D.; Mitchell, N.J. The southern stratospheric gravity wave hot spot: Individual waves and their momentum fluxes measured by COSMIC GPS-RO. *Atmos. Chem. Phys.* **2015**, *15*, 7797–7818. [[CrossRef](#)]
26. Sam-Khaniani, A. Long-term evaluation of temperature profiles derived from space-based GPS meteorology with radiosonde measurements over Iran. *Earth Obs. Geomat. Eng.* **2020**, *4*, 1–12. [[CrossRef](#)]
27. Šácha, P.; Kuchař, A.; Jacobi, C.; Pišoft, P. Enhanced internal gravity wave activity and breaking over the northeastern Pacific–eastern Asian region. *Atmos. Chem. Phys.* **2015**, *15*, 13097–13112. [[CrossRef](#)]
28. Leroy, S.S.; Ao, C.O.; Verkhoglyadova, O.P. Temperature trends and anomalies in modern satellite data: Infrared sounding and GPS radio occultation. *J. Geophys. Res. Atmos.* **2018**, *123*, 11431–11444. [[CrossRef](#)]
29. Hersbach, H.; Bell, B.; Berrisford, P.; Hirahara, S.; Horányi, A.; Muñoz-Sabater, J.; Nicolas, J.; Peubey, C.; Radu, R.; Schepers, D.; et al. The ERA5 global reanalysis. *Q. J. R. Meteorol. Soc.* **2020**, *146*, 1999–2049. [[CrossRef](#)]
30. Wang, X.; Xue, Z.G.; Du, X.Y.; Yan, W. Method of GPS-LEO Occultation Measurements of the Atmosphere. *GNSS World China* **2002**, *27*, 14–20. [[CrossRef](#)]
31. Hu, X.; Zeng, Z.; Zhang, X.X.; Zhang, D.Y.; Xiao, C.Y. Atmospheric inversion methods of GPS radio occultation. *Chin. J. Geophys.* **2005**, *48*, 768–774. (In Chinese) [[CrossRef](#)]
32. Ern, M.; Preusse, P.; Alexander, M.J.; Warner, C.D. Absolute values of gravity wave momentum flux derived from satellite data. *J. Geophys. Res. Atmos.* **2004**, *109*, D20103. [[CrossRef](#)]
33. Ratnam, M.V.; Tetzlaff, G.; Jacobi, C. Global and seasonal variations of stratospheric gravity wave activity deduced from the CHAMP/GPS satellite. *J. Atmos. Sci.* **2004**, *61*, 1610–1620. [[CrossRef](#)]
34. Xu, X.; Yu, D.; Luo, J. The spatial and temporal variability of global stratospheric gravity waves and their activity during sudden stratospheric warming revealed by COSMIC measurements. *Adv. Atmos. Sci.* **2018**, *35*, 1533–1546. [[CrossRef](#)]
35. Xu, X.; Yu, D.; Luo, J. Seasonal variations of global stratospheric gravity wave activity revealed by COSMIC RO data. In *2017 Forum on Cooperative Positioning and Service (CPGPS)*; IEEE: New York, NY, USA, 2017; pp. 85–89. [[CrossRef](#)]
36. Miyahara, S.; Hayashi, Y.; Mahlman, J.D. Interactions between gravity waves and planetary-scale flow simulated by the GFDL “SKYHI” general circulation model. *J. Atmos. Sci.* **1986**, *43*, 1844–1861. [[CrossRef](#)]
37. Yu, D.C. The Climatology and Variability of Stratospheric Gravity Waves Based on COSMIC Radio Occultation Observations. Master’s Thesis, Wuhan University, Wuhan, China, 2018.
38. Khaykin, S.M.; Hauchecorne, A.; Mzé, N.; Keckhut, P. Seasonal variation of gravity wave activity at midlatitudes from 7 years of COSMIC GPS and Rayleigh lidar temperature observations. *Geophys. Res. Lett.* **2015**, *42*, 1251–1258. [[CrossRef](#)]
39. Steiner, A.K.; Kirchengast, G.; Lackner, B.C.; Pirscher, B.; Borsche, M.; Foelsche, U. Atmospheric temperature change detection with GPS radio occultation 1995 to 2008. *Geophys. Res. Lett.* **2009**, *36*, L18702. [[CrossRef](#)]
40. Schmidt, T.; Wickert, J.; Haser, A. Variability of the upper troposphere and lower stratosphere observed with GPS radio occultation bending angles and temperatures. *Adv. Space Res.* **2010**, *46*, 150–161. [[CrossRef](#)]